scientific reports

Check for updates

OPEN

Environment-adaptive track mechanism with continuously transformable grousers

Hanbom Kim[1], Yongho Kwon[1], Hojoon Seo[1], Jeongmo Yang[1], Seungjun Kim[1], Jong-Won Kim[2] & TaeWon Seo[1]✉

This study presents EATbot, an environment-adaptive tracked robot featuring an arc-grouser mechanism that continuously modulates grouser protrusion and the resulting ground-contact profile rather than altering the overall track posture. Conventional fixed-profile tracks must compromise grouser geometry because low-profile treads improve flat-ground smoothness, whereas highly protruded grousers improve rough-terrain and stair-edge engagement. To address this fixed-grouser-profile trade-off, the proposed mechanism continuously modulates the protrusion of arc-shaped grousers over the range from a retracted low-profile configuration to a maximum-protrusion high-engagement configuration within a single track module. A kinematic model and virtual-work-based torque formulation were developed to characterize grouser protrusion behavior and load-dependent actuation requirements. The arc-grouser geometry was designed to maximize usable protrusion within chain discretization, internal interference, packaging, and actuator constraints, while a non-collinear structural offset was incorporated to prevent simultaneous dead-center locking during continuous transformation. Stair-climbing tests verified the predicted climbable domain and demonstrated successful ascent up to a maximum equivalent inclination of 48.85°. Driving stability experiments showed that the retracted configuration decreased RMS vibration by 5.1% on flat terrain, whereas the maximum-protrusion configuration reduced vibration by 87.9% on rough terrain. Payload transformation tests up to 40 kg further demonstrated practical high-load operation. These results indicate that continuous grouser-profile transformation can mitigate the fixed-profile trade-off between flat-ground smoothness and stair/rough-terrain engagement while preserving the continuous-contact characteristics of tracked locomotion.

Ground mobile robots are commonly categorized into legged, wheeled, and tracked mechanisms[1]. Legged systems offer strong terrain adaptability but require complex multi-actuator control[2,3]. Wheeled robots are efficient on structured surfaces yet are fundamentally limited in obstacle-crossing capability by wheel diameter[4,5]. Tracked mechanisms provide high traction and stable mobility on soft or uneven terrain[6,7], and are widely adopted in surveillance, rescue, planetary exploration, and hazardous environments[8–14].

Despite their advantages, conventional tracked systems face a fixed-grouser-profile trade-off in heterogeneous terrain. In tracked locomotion, the grouser is the ground-contact element that directly governs traction, mechanical interlocking, and terrain engagement. Previous terramechanics studies have shown that grouser geometry strongly affects wheel/track–terrain interaction, including stress distribution, soil failure behavior, slip, and traction generation[15–17]. A large grouser protrusion improves engagement with rough terrain or stair-like discontinuities, but in a fixed-profile track the same protruded geometry must also be used on flat ground, where it can increase vibration, impact loading, wear, and local stress concentration. Thus, practical tracks and tread-like contact surfaces generally adopt shallow or moderate protrusions as a compromise between rough-terrain engagement and flat-ground smoothness. Recent adaptive-grouser wheel research similarly showed that no single grouser height minimized slip across different terrains[18]; however, continuously transformable grouser-profile mechanisms for continuous-track platforms remain underexplored.

Previous reconfigurable tracked robots have mainly improved terrain adaptability by changing the global track posture, adding flipper-type modules, or modifying the overall locomotion configuration[19–21]. In contrast, this study focuses on the grouser itself rather than the global track shape. The proposed mechanism continuously modulates the protrusion/contact profile of arc-shaped grousers over the range from a retracted state to a maximum-protrusion state, enabling a continuous spectrum of contact profiles within a single track module.

[1]School of Mechanical Engineering, Hanyang University, Seoul 04763, Republic of Korea. [2]Feasix AI Co.,Ltd., Seongnam 08826, Republic of Korea. ✉email: taewonseo@hanyang.ac.kr

This approach differs from both fixed-profile tracks and binary deployable protrusions because the track–terrain contact profile can be adjusted continuously without replacing the track or changing the locomotion module.

To realize this concept, this study proposes the **Environment-Adaptive Tracked robot (EATbot)**, a tracked platform equipped with continuously transformable arc grousers driven by an eccentric non-collinear coupled linkage. In this work, "environment-adaptive" refers to the hardware-level ability to continuously adjust the track–terrain contact profile through grouser-profile transformation. The arc-grouser geometry was designed to maximize usable protrusion while satisfying chain-pitch discretization, internal interference, packaging, grouser curvature, and actuator feasibility constraints. The resulting maximum-protrusion state provides stair-edge engagement and distributed load transfer across multiple contact regions, enabling stair climbing up to a maximum equivalent inclination of $48.85°$, as verified experimentally.

The main contributions of this work are:

1. A protrusion-maximized continuously transformable arc-grouser mechanism for tracked locomotion. The proposed mechanism continuously modulates grouser protrusion and the resulting track–terrain contact profile over the full range from the retracted state to the maximum-protrusion state. The arc-grouser geometry is designed to maximize the attainable protrusion range within a compact track module.
2. A mechanism-level design and analysis for robust continuous grouser transformation. The arc-grouser geometry and eccentric guide mechanism are designed under chain, interference, packaging, curvature, and actuator constraints, while the eccentric non-collinear coupled linkage separates the dead-center input angles of the coupled sub-loops.
3. A single-platform experimental characterization of fixed-grouser-profile trade-off mitigation. Stair-climbing, flat/rough terrain vibration, and payload transformation tests verify that the proposed mechanism can realize both flat-ground-friendly and high-engagement contact profiles, including stair climbing at an equivalent inclination of $48.85°$.

Robot mechanism design

The overall configuration of EATbot is presented in Fig. 1. The robot has a footprint of 726×412 mm, a height of 227 mm, and a total mass of 41.78 kg. These dimensions were selected to balance indoor maneuverability with longitudinal stability during steep ascent, while remaining compatible with standard urban stair geometry.

The width of 412 mm satisfies minimum clearance requirements for accessible indoor facilities [22,23], enabling operation in narrow corridors. A length-to-height ratio of approximately 3.2:1 maintains the center of gravity at approximately 110 mm, improving static stability on inclined surfaces [24]. In addition, the total track length allows the robot to span at least two standard stair steps, i.e., a 300 mm tread and a 180 mm riser [25], which increases the probability of multi-point engagement and reduces pitch instability during transitions.

The track module adopts a dual-path actuation architecture, as shown in the exploded view in Fig. 2. Each side integrates one propulsion actuator for sprocket driving and a separate actuator for grouser-profile transformation. This mechanical decoupling is important because propulsion torque is mainly governed by slope and payload, whereas transformation torque depends on linkage transmission, grouser configuration, and contact loading. Separating the two actuation paths reduces interference between locomotion and reconfiguration and improves robustness during high-load stair climbing.

The propulsion system employs a 169 mm diameter sprocket and dual-strand hollow-pin #40 chains arranged in a sandwich configuration. Arc-shaped grousers are mounted between the parallel chains and supported at both ends, which improves symmetric load distribution and torsional rigidity when the robot engages stair edges. To avoid ambiguity in actuator indexing, the eccentric cam transformation motors are denoted as M1 and M2, while the propulsion motors are denoted as M3 and M4 (Fig. 2); the corresponding motor current signals are defined as $I_{\mathrm{M}i}$ for $i \in \{1, 2, 3, 4\}$.

The transformation mechanism is based on an internally mounted eccentric guide, as shown in Fig. 3a. Each arc grouser is connected to the dual-strand chains through a central pivot shaft, while a guide roller attached to the grouser follows the eccentric guide path. Rotation of the eccentric guide changes the radial offset between the outer chain path and the internal guide path, inducing controlled rotation of the grousers about their pivot shafts. As a result, the grouser profile can be continuously extended or retracted relative to the baseline track shape.

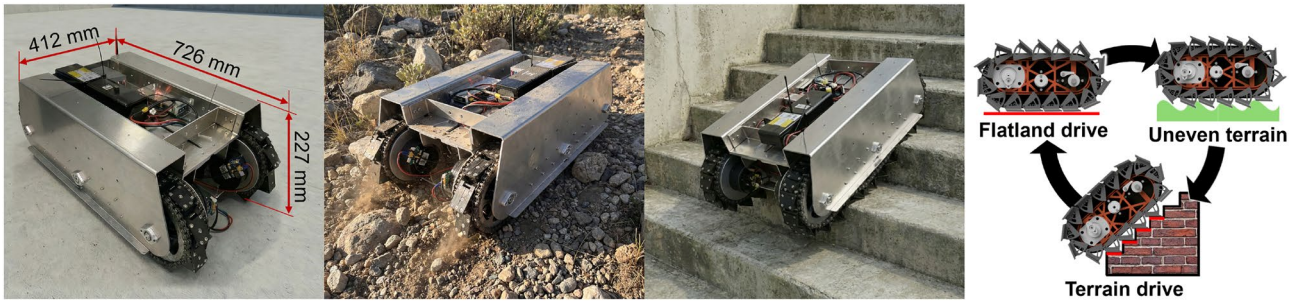

Fig. 1. Prototype specifications and mode transitions. Diverse applications for navigating unstructured environments, including stairs and gravel terrain.

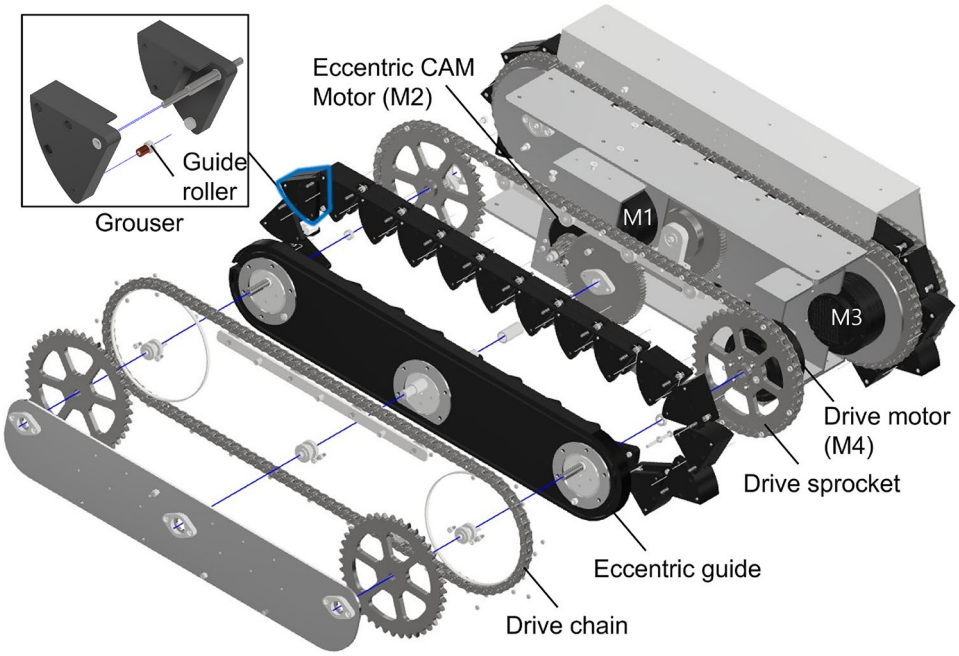

Fig. 2. Exploded view of the track module. The assembly shows the integration of the driving sprockets, internal cam-linkage, and modular grouser units for continuous transformation.

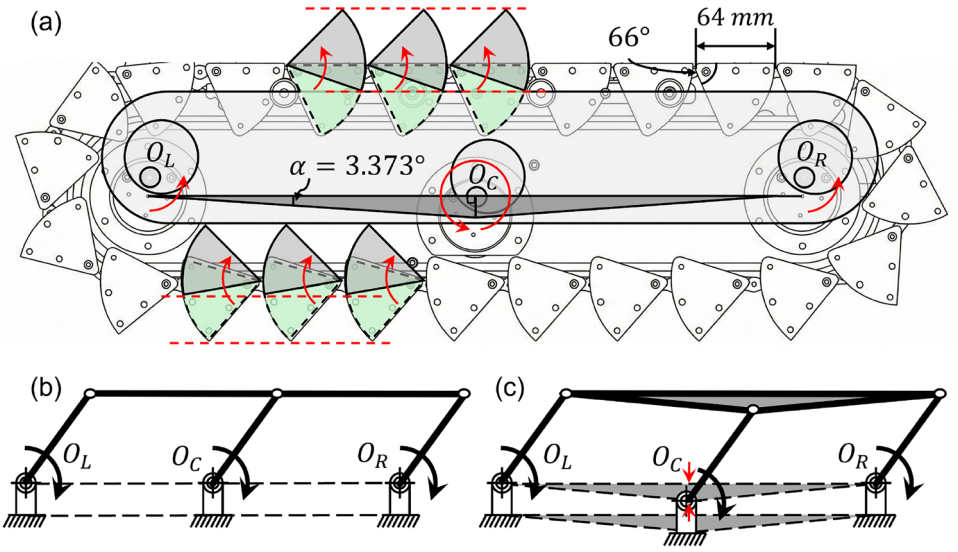

Fig. 3. Cross-sectional view and simplified model of the transformation linkage. (**a**) Implemented mechanism, where the eccentric guide modulates the radial offset to rotate the arc grousers about their pivot shafts. The three shaft centers O_L, O_C, and O_R form a non-collinear triangular axis arrangement with $\alpha = 3.373°$. (**b**) Collinear arrangement ($\alpha = 0°$), where simultaneous dead-center configurations can occur. (**c**) Proposed offset arrangement, where the central shaft offset separates the dead-center input angles of the coupled sub-loops.

The implemented linkage should be distinguished from a conventional single four-bar linkage. The centrally driven eccentric shaft O_C synchronizes the motion of the left and right follower shafts, O_L and O_R, so the mechanism can be interpreted as two coupled four-bar-like sub-loops sharing O_C. If the three shaft centers are collinear, as in Fig. 3b, the two sub-loops can have identical dead-center input angles, which may cause simultaneous dead-center configurations and discontinuous motion transmission [26,27]. Therefore, O_C was vertically offset from the line connecting O_L and O_R, forming the non-collinear triangular axis arrangement shown in Fig. 3c. The resulting structural offset angle is $\alpha = 3.373°$, which separates the dead-center input angles of the coupled sub-loops.

The resulting profile transformation is illustrated by the prototype sequence in Fig. 4. Starting from the retracted configuration in Fig. 4a, the grousers are continuously deployed through the protrusion range in Fig. 4b–d and reach the maximum-protrusion configuration in Fig. 4e. The subsequent frames in Fig. 4f–h show the reverse transition toward the retracted configuration, demonstrating continuous and reversible profile modulation in the prototype. This sequence also clarifies that the proposed mechanism is not a binary deployable grouser, but a continuously transformable grouser-protrusion mechanism capable of realizing arbitrary configurations within the attainable protrusion range.

Each arc grouser has a radius of 64 mm and a central angle of 66°. Under maximum eccentricity, the mechanism provides substantial protrusion while remaining compatible with internal guide geometry and chain constraints. Together, the dual-path actuation architecture, eccentric-guide-based profile transformation, and non-collinear coupled linkage establish the mechanical basis for hardware-level adaptation of the track–terrain contact profile.

Kinematic and geometric analysis

This section establishes the geometric relationship between the eccentric cam rotation and the resulting grouser protrusion. Because the achievable protrusion directly determines the effective transmission radius and the maximum climbable inclination, it is necessary to formulate an explicit mapping from cam angle to grouser displacement. The derived relationship provides the geometric foundation for both the stair-climbing limit analysis and the torque formulation presented in the following sections.

The profile transformation of EATbot is a single-degree-of-freedom system governed by the eccentric cam rotation angle θ_1. As illustrated in Fig. 5, the grouser orientation is determined by the relative offset between the outer chain path and the inner guide rail. Because the grouser rotates about its pivot while its guide roller is constrained by the eccentric guide, the cam angle defines the effective protrusion height along the required transformation path. This mapping is the basis for both the kinematic analysis and the subsequent torque estimation.

The radial gap, residual grouser rotation, and protrusion height are expressed as

$$d(\theta_1) = R - r - l_{link}\cos\theta_1, \tag{1}$$

$$\theta_2(\theta_1) = \arcsin\left(\frac{d(\theta_1)}{r_{gr}}\right), \tag{2}$$

$$h(\theta_1) = r_{gr}\sin(\theta_{gr} - \theta_2(\theta_1)), \tag{3}$$

which together define the mapping from cam rotation to grouser protrusion (Fig. 5). Here, R and r denote the outer sprocket radius and the inner guide radius, respectively, and r_{gr} and θ_{gr} represent the grouser curvature radius and nominal central angle. The parameter l_{link} denotes the effective eccentric-link length in the simplified planar model, corresponding to the distance from the eccentric cam center to the guide-roller driving point. This length determines the amplitude of radial-gap modulation between the outer chain path and the inner guide rail. The term $d(\theta_1)$ captures how the eccentric motion changes the radial separation between the chain path and the guide path, while $\theta_2(\theta_1)$ represents the induced grouser rotation required to satisfy the geometric constraint.

The non-collinear offset in Fig. 3c prevents the two coupled sub-loops from reaching their dead-center configurations at the same input angle. Let L be the distance between O_L and O_R, and let h_{off} be the vertical offset of O_C from the line connecting them. The structural offset angle is

$$\alpha = \tan^{-1}\left(\frac{h_{\text{off}}}{L/2}\right). \tag{4}$$

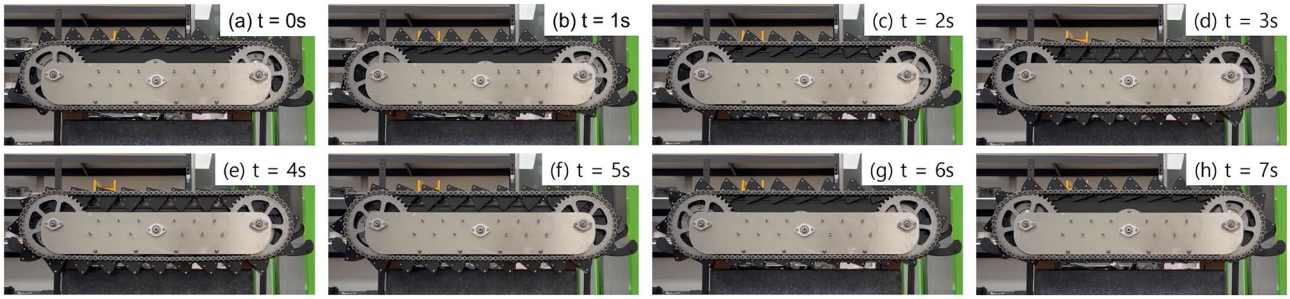

Fig. 4. Time-lapse sequence of the continuous grouser-profile transformation in the prototype. (**a**) Retracted configuration, (**b**–**d**) progressive deployment, (**e**) maximum-protrusion configuration, and (**f**–**h**) progressive retraction. As the internal eccentric guide rotates, the guide rollers follow the eccentric guide path and the arc grousers continuously protrude from and retract toward the baseline track profile. This sequence visually demonstrates the continuous and reversible profile modulation achieved by the proposed track module.

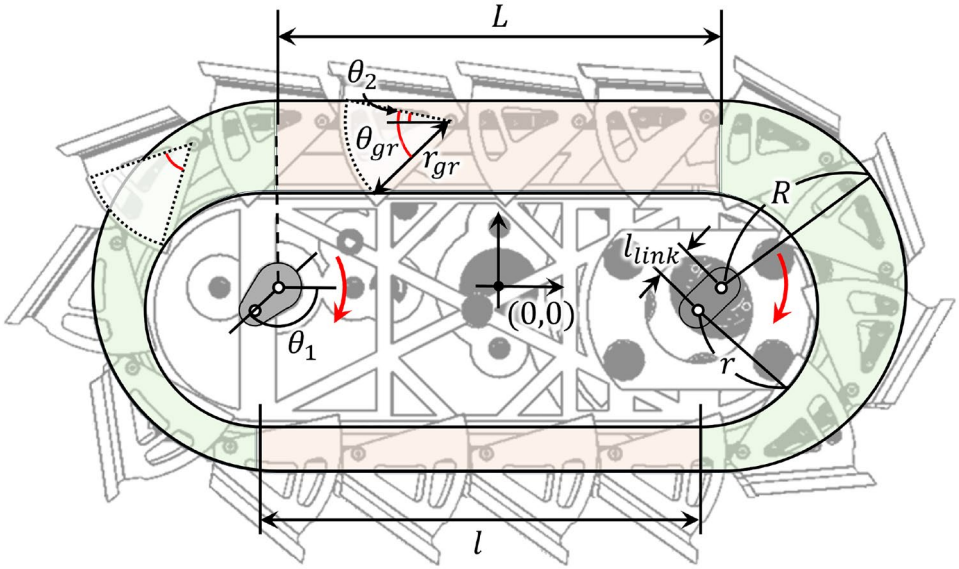

Fig. 5. Kinematic parameters and coordinate system of the transformable track. The diagram defines the geometric variables used for piecewise protrusion analysis in the straight and semi-circular regions.

In the collinear case in Fig. 3b, $\alpha = 0^\circ$, and the left and right sub-loops have identical dead-center input angles. With the proposed offset arrangement in Fig. 3c, these input angles are separated by 2α. For the implemented design,

$$\alpha = 3.373^\circ, \qquad 2\alpha = 6.746^\circ. \tag{5}$$

For a symmetric two-loop approximation, the separation of the two dead-center directions can be expressed using the following geometric index:

$$S_{\mathrm{dc}} = 2\sin^2\alpha. \tag{6}$$

This index is not intended as a general singularity measure for arbitrary planar linkages. Instead, it quantifies whether the dead-center input directions of the two coupled sub-loops coincide in the implemented shaft arrangement. Thus, $S_{\mathrm{dc}} = 0$ for the collinear case, indicating simultaneous dead-center alignment, whereas the implemented offset gives

$$S_{\mathrm{dc}} = 2\sin^2(3.373^\circ) = 0.00692 > 0. \tag{7}$$

Therefore, the selected structural offset provides a finite geometric separation against simultaneous dead-center configurations while remaining within the available packaging space.

Geometric parameters were selected by intersecting chain discretization, internal transport/interference, and outer packaging/mass constraints (Figs. 6, 7). A hollow-pin #40 chain sets the pitch at $P = 12.7$ mm, which discretizes feasible grouser spacing and strongly constrains candidate radii through integer pitch relationships. The inner guide radius is bounded mainly by inter-grouser interference and internal transport feasibility (Fig. 6a), yielding

$$r \geq 45\,\mathrm{mm}. \tag{8}$$

If r is smaller than this bound, adjacent grousers and rollers may jam or collide during transformation, and the inner guide may violate the minimum clearance required for assembly.

The outer sprocket radius is bounded by packaging and mass growth (Fig. 6b), resulting in

$$55\,\mathrm{mm} \leq R \leq 96.3\,\mathrm{mm}. \tag{9}$$

A larger R increases the available deformation capability by enlarging $(R - r)$, but it also increases structural load, inertia, and overall volume, which are undesirable for compact indoor platforms. Within the feasible region (Fig. 7), the deformation capability increases with $(R - r)$, motivating the selection of r_{gr} as large as allowed by chain pitch and interference limits while keeping R within the practical packaging envelope.

A standard 40-tooth sprocket fixes $R = 82.5$ mm, and a five-pitch multiple yields $r_{gr} = 64$ mm. The corresponding inner guide radius is $r = 51.4$ mm, completing the finalized parameter set used in the subsequent analysis and experiments. These parameters represent a balanced design point that satisfies discrete chain constraints while preserving sufficient protrusion range for steep stair engagement. In particular, the

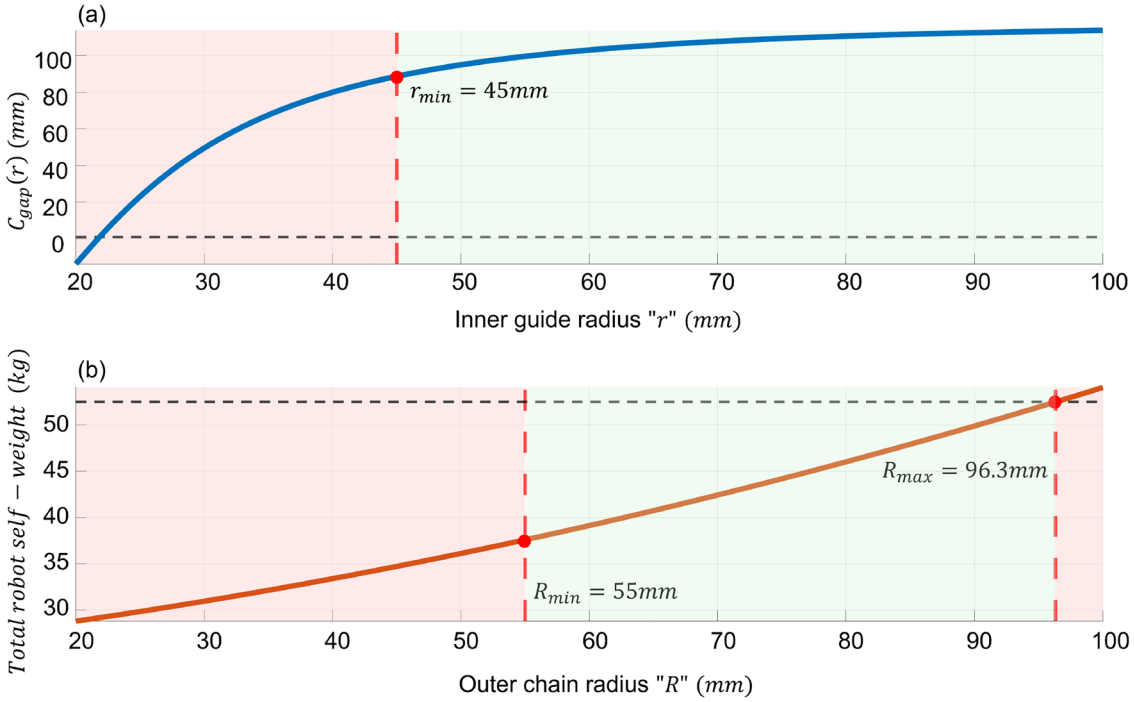

Fig. 6. Constraint-based determination of structural radii. (**a**) Lower bound of the inner guide radius r from transport and interference constraints (shaded region: infeasible). (**b**) Feasible range of the outer sprocket radius R from packaging and mass constraints, with R_{min} and R_{max} indicated.

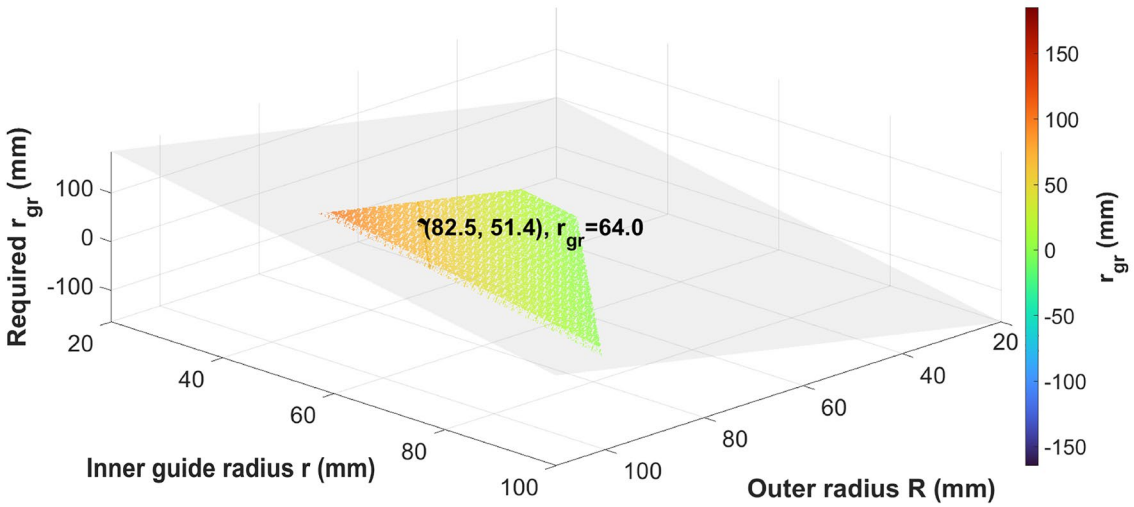

Fig. 7. Design map for r_{gr} optimization. The feasible region is bounded by the inner guide radius constraint (to avoid jamming) and the outer sprocket radius limit (to minimize mass and structural load).

resulting maximum protrusion determines the effective radius r_{eff} in the propulsion model and leads to the experimentally validated maximum inclination of $\beta_{\max} = 48.85^{\circ}$ discussed in Experiment 1.

Dynamic and load transmission analysis

The propulsion requirement of EATbot is analyzed under two representative operating conditions: an equivalent inclined plane and discrete stair engagement, illustrated in Fig. 8a,b, respectively. Although stair climbing involves multiple discrete contacts, the dominant global torque demand is governed by the gravitational component acting along the direction of motion. Under quasi-static conditions, both cases reduce to the same fundamental relationship,

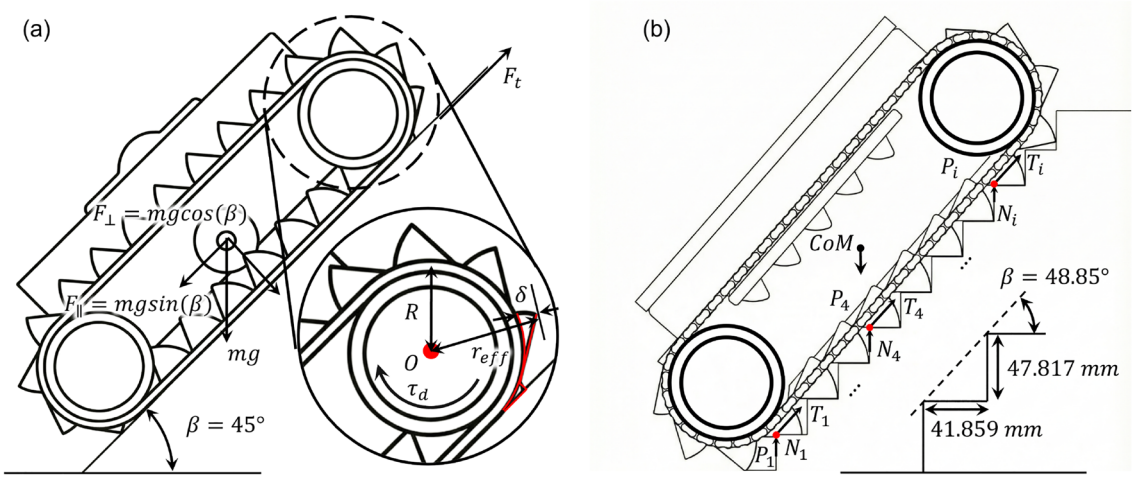

Fig. 8. Force equilibrium and contact models of the transformable track. (**a**) Inclined-plane model at $\beta = 45°$, illustrating the effective radius r_{eff} and driving torque τ_d. (**b**) Distributed multi-contact model at $\beta = 48.85°$, showing the reaction forces (N_i, T_i) at multiple engagement points P_i.

$$\tau = mg \sin\beta \, r_{\text{eff}}, \tag{10}$$

where β is the equivalent inclination angle and r_{eff} is the effective transmission radius including grouser protrusion. This expression shows that propulsion torque increases monotonically with both slope angle and protrusion height, establishing a direct geometric link between transformation capability and maximum climbable inclination.

The distinction between Fig. 8a,b lies not in the magnitude of the global torque but in the contact topology. The inclined-plane model provides a conservative lower-bound estimate of the required driving torque. In contrast, the stair model captures the distributed, multi-point engagement between successive grousers and stair edges. Such distributed contact reduces local reaction peaks and improves pitch stability through load sharing, which becomes particularly important near the geometric limit $\beta_{\max} = 48.85°$.

Comparison with actuator specifications indicates that the experimental configuration operates within rated torque capacity under the tested payloads. Extreme hypothetical overload conditions would exceed motor limits, confirming that propulsion performance at high inclination is actuator-limited rather than structurally limited.

The transformation subsystem is driven by an eccentric non-collinear coupled linkage (Fig. 3a). Under quasi-static conditions, the required input torque follows from virtual work,

$$\tau_{in} = F_{resist} \frac{dh}{d\theta_1}, \tag{11}$$

where $\frac{dh}{d\theta_1}$ represents the kinematic transmission ratio between cam rotation and grouser displacement. Because the linkage incorporates the non-collinear structural offset shown in Fig. 3c, simultaneous dead-center configurations are avoided in the simplified two-loop model of the implemented mechanism. This allows the transformation torque to be transmitted continuously along the required grouser-transformation path, including the maximum-protrusion state.

CAE-based structural verification

To verify the structural feasibility of the proposed track-module design, nonlinear static finite element analysis was performed under representative support conditions with fully deployed grousers. The analysis considered not only distributed-contact states, but also a conservative two-point contact state that can occur during stair ascent, stair descent, or rough-terrain transition.

Three representative support conditions were considered. The first condition represents flat-ground distributed support, in which multiple deployed grousers share the external load. The second condition represents stair-contact climbing support, in which the deployed grousers engage with stair edges during climbing. The third condition represents a two-point contact support state, in which the external load is carried by only a small number of grousers. Although the exact body angle of this state depends on stair geometry and contact sequence, such an intermediate support state can occur during obstacle negotiation and was therefore included as a conservative load case.

Figure 9a–c shows the representative support conditions considered in the finite element analysis. The detailed contour results in Fig. 9d,e correspond to the two-point contact support case under a conservative overload condition. Under this condition, local deformation and stress are concentrated near the ground-contact grouser and rotating guide roller pin region.

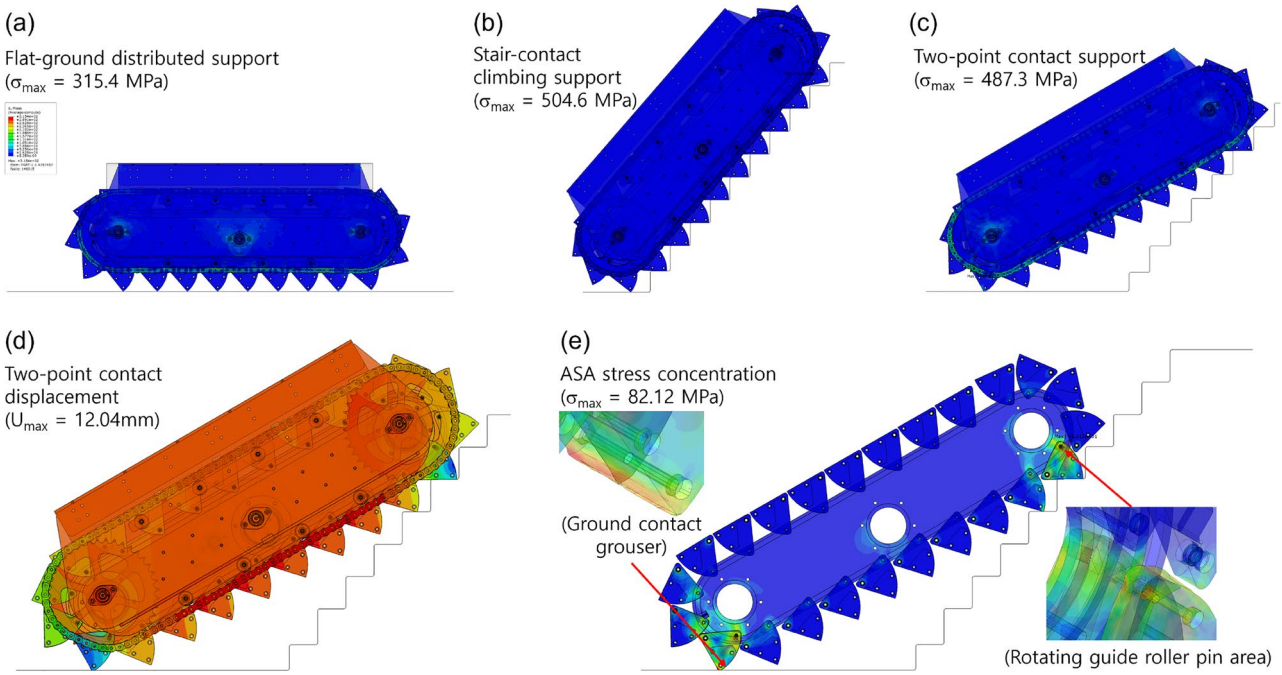

Fig. 9. CAE-based structural verification of the proposed track-module design with fully deployed grousers. (**a**) Flat-ground distributed support condition, where multiple deployed grousers share the external load. (**b**) Stair-contact climbing support condition, where the deployed grousers engage with stair edges during climbing. (**c**) Two-point contact support condition, representing a conservative support state that can occur during stair ascent, descent, or rough-terrain transition. (**d**) Total displacement contour of the two-point contact support case under the conservative overload condition. (**e**) von Mises stress distribution of the ASA grouser components under the same two-point contact condition. The results show that local deformation and stress are concentrated near the ground-contact grouser and rotating guide roller pin region under the two-point contact support condition.

Support condition	U_{max} (mm)	σ_{max}^{whole} (MPa)	$PEEQ_{max}^{whole}$ (–)	σ_{max}^{ASA} (MPa)	$PEEQ_{max}^{ASA}$ (–)	Dominant weak region
Flat-ground distributed support	3.134	315.4	0.2519	73.69	0.1745	Roller-guide pin/main shaft region
Stair-contact climbing support	3.625	504.6	0.8588	73.88	0.1741	Grouser connecting pin/main shaft supporting region
Two-point contact support	12.04	487.3	2.192	82.12	0.8211	Ground-contact grouser/rotating guide roller pin region

Table 1. Finite element results for representative support conditions with fully deployed grousers under the same conservative overload condition.

The numerical results are summarized in Table 1. To isolate the effect of support configuration, the three representative cases were evaluated under the same conservative overload condition. The distributed-support cases showed relatively smaller deformation because the load was shared by multiple deployed grousers, whereas the two-point contact support condition produced the largest displacement and equivalent plastic strain due to localized load transfer. Therefore, the structural limitation of the proposed mechanism is governed primarily by localized deformation around the grouser–guide interface and pin-supported load-transfer path, rather than by global frame collapse of the track module.

In addition to the support-condition comparison, a displacement-controlled load analysis was performed for the two-point contact support condition to estimate the allowable reaction load of the ASA grouser components. During this analysis, the maximum equivalent plastic strain in the ASA parts was monitored while increasing the imposed displacement. Using $PEEQ = 0.02$ as the allowable plastic strain criterion for the ASA material, the corresponding reaction load was estimated to be approximately 2400 N. This value was used as a conservative structural reference for assessing the load margin of the grouser mechanism, not as an experimentally verified ultimate payload capacity.

The subsequent payload transformation test was conducted to verify whether the mechanism can complete the required transformation under a practical self-weight-level payload, rather than to determine the ultimate failure load.

Experimental characterization

This section quantitatively characterizes the proposed continuously transformable arc-grouser mechanism through three complementary evaluations: geometric feasibility, terrain-dependent driving stability, and load-bearing transformation capability. First, the climbable stair domain is formulated and tested to examine whether the achievable protrusion range translates into practical stair-climbing performance. Second, terrain-dependent driving stability is quantified to evaluate the fixed-grouser-profile trade-off using same-platform locked configurations. Finally, payload-based transformation tests estimate actuator torque requirements and assess practical transformation feasibility under self-weight-level loading. Together, these experiments characterize the performance, trade-off mitigation, and practical feasibility of the proposed mechanism.

Climbable stair domain analysis

The climbable stair region shown in Fig. 10 is formulated in the (h_s, w_s) domain, where h_s and w_s denote the riser height and tread depth, respectively. The effective stair diagonal is defined as

$$R_c = \sqrt{h_s^2 + w_s^2}, \tag{12}$$

representing the geometric spacing between successive stair edges.

Let P be the chain pitch and n_g the number of pitches per grouser. The spacing between adjacent grousers is $s_g = n_g P$. Stair compatibility requires approximate alignment between the stair diagonal and an integer multiple of the grouser spacing, expressed as

$$|R_c - k s_g| \le \Delta_c, \qquad k \le k_{\max}, \tag{13}$$

where Δ_c denotes an admissible tolerance.

Unlike fixed-grouser systems, the transformable grousers establish distributed contact, allowing tolerance in diagonal mismatch. If ℓ_e denotes the admissible engagement window for a single grouser, simultaneous engagement of at least two grousers yields

$$\Delta_c \approx 2 r_{\text{eff}} \phi_e, \tag{14}$$

where ϕ_e represents the effective contact angle under distributed interaction.

In addition to discrete engagement, geometric feasibility requires that the equivalent inclination

$$\beta = \tan^{-1}\left(\frac{h_s}{w_s}\right) \tag{15}$$

does not exceed the maximum transformable limit $\beta_{\max}$.

The climbable stair domain $\mathcal{S}$ is therefore defined as

$$\mathcal{S} = \left\{ (h_s, w_s) \,\middle|\, \exists k \le k_{\max} \text{ such that } \left|\sqrt{h_s^2 + w_s^2} - k s_g\right| \le \Delta_c,\ h_s \le w_s \tan\beta_{\max} \right\}. \tag{16}$$

The shaded region in Fig. 10 corresponds to $\mathcal{S}$, with experimentally tested staircases overlaid for validation.

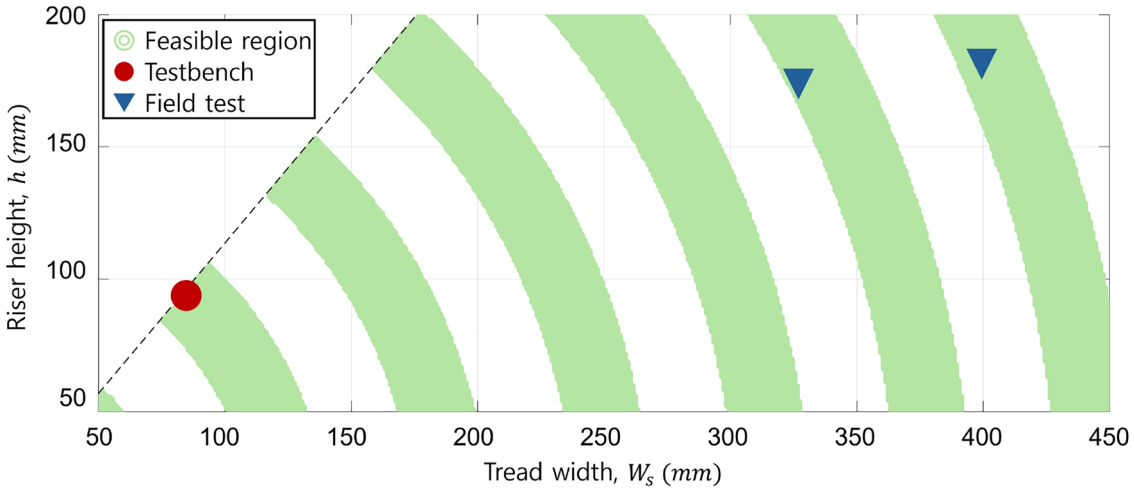

Fig. 10. Climbable stair domain of the proposed robot in the (h_s, w_s) space. The shaded region represents geometries satisfying both the discrete grouser-engagement condition and the maximum inclination constraint. Experimentally tested staircases are overlaid as markers.

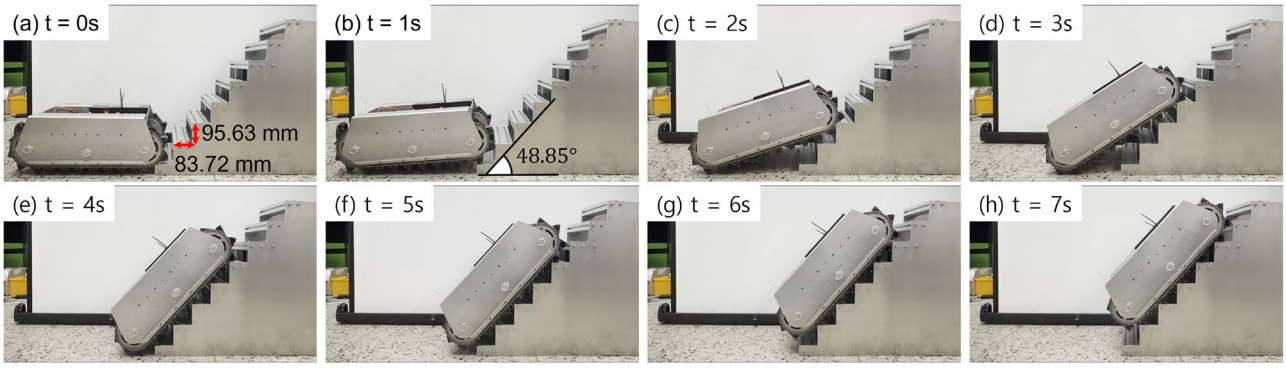

Fig. 11. Stair-climbing test on the maximum-slope test bench. Time-lapse frames illustrate the ascent from the initial contact to successful climb completion.

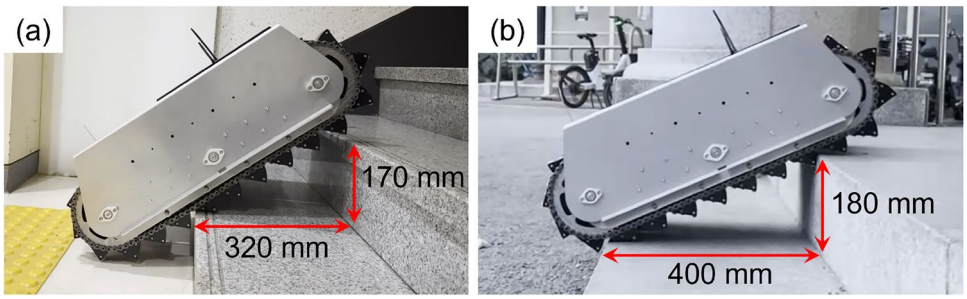

Fig. 12. Field stair-climbing tests on real staircases. Stair sizes: (**a**) 320×170 mm^2 (tread×riser), (**b**) 400×180 mm^2.

Experiment 1: stair-climbing capability

Stair-climbing experiments were conducted to evaluate the theoretically predicted climbable domain shown in Fig. 10. The stair geometry is represented in the (h_s, w_s) space following established stair-domain formulations for tracked climbing systems[25]. The maximum geometric inclination determined by the transformable grouser configuration is $\beta_{\max} = 48.85°$, corresponding to the maximum protrusion state.

To evaluate this limit experimentally, a dedicated maximum-slope test bench was fabricated near $\beta_{\max}$ (Fig. 11). The inclination angle is explicitly indicated in Fig. 11b at $t = 1$ s to visualize the maximum-slope condition. The robot successfully ascended the maximum-angle staircase without structural failure or actuator saturation, demonstrating that the geometric transformation range directly translates into practical climbing capability.

Both the geometrically matched stair and its integer-multiple configuration were tested. Successful ascent in both cases confirms that distributed multi-point engagement compensates for diagonal mismatch during step transitions, validating the tolerance formulation derived in the climbable domain analysis.

Field experiments were further performed on two real staircases with moderate inclinations (Fig. 12). Both geometries fall within the predicted feasible region and were climbed without manual adjustment of the transformation state.

To contextualize the maximum-slope stair-climbing result, Table 2 compares representative stair-climbing robots with explicitly reported stair geometries. A recent review classified stair-climbing robots by locomotion mechanism and suggested stair dimension, vertical climbing speed, and mechanism complexity as useful evaluation criteria [36]. In this study, the equivalent stair angle was calculated as $\beta_{\text{eq}} = \tan^{-1}(h_s/w_s)$ when both riser height h_s and tread depth w_s were available. Systems reporting only single-obstacle height or wheel-radius-normalized obstacle height were excluded to avoid unsupported angle estimation.

As shown in Table 2, the maximum-slope test condition of EATbot corresponds to an equivalent inclination of $48.85°$, which is higher than the reported equivalent stair angles of the representative stair-climbing robots listed in the table. This comparison does not imply a universal ranking across all stair-climbing systems because robot scale, locomotion principle, control strategy, and stair geometry differ among studies. Rather, it provides a quantitative reference showing that the tested condition lies in a highly steep range.

The review literature further indicates that stair-climbing robots should be evaluated not only by climbable stair size but also by mechanism complexity and vertical climbing speed [36]. From this viewpoint, EATbot is positioned as a tracked platform that retains the structural simplicity and continuous contact characteristics of tracks while extending the usable stair-inclination range through continuous grouser-profile transformation.

System	Mechanism	Reported stair condition	Feature	β_{eq}
EATbot	Tracked robot with transformable arc grousers	Maximum-slope stair test bench	Continuous grouser-profile transformation	48.85°
STEP [19]	2-DOF transformable wheel	$h_s = 100$–180 mm, $w_s = 260$–300 mm	Active wheel-shape transformation	18.4° –34.7°
Quattroped [28]	Leg–wheel transformable robot	$h_s = 150$–170 mm, $w_s = 250$–300 mm	Active wheel–leg transformation	26.6° –34.2°
α-WaLTR [29]	Adaptive wheel–leg robot	$h_s = 180$ mm, $w_s = 290$ mm	Passive wheel–leg transformation	31.8°
GerWalk [30]	Elastic spoke rimless-wheel robot	$h_s = 170$ mm, $w_s = 280$ mm	Elastic spoke wheel	31.3°
Kinect-based tracked robot [31]	Reconfigurable tracked robot	$h_s = 170$ mm, $w_s = 290$ mm	Track posture reconfiguration	30.4°
Segmented wheel robot [32]	Segmented transformable wheel	$h_s = 64$ mm, $w_s = 110$ mm	Segmented wheel transformation	30.2°
WAVES [25,33]	Soft-material walking-type stair climber	$h_s = 180$ mm, $w_s = 310$ mm	Passive soft-foot deformation	30.1°
Active rotary-legs mobility [34]	Four-bar rotary-leg mobility	$h_s = 125$ mm, $w_s = 300$ mm	Gas-spring rotary legs	22.6°
MSRox [35]	Star-wheel robot	$h_s = 140$ mm, $w_s = 370$ mm	Star-wheel rotation	20.7°

Table 2. Comparison of reported stair-climbing conditions of representative stair-climbing robots. The equivalent stair angle was calculated as $\beta_{eq} = \tan^{-1}(h_s/w_s)$, where h_s and w_s denote riser height and tread depth, respectively.

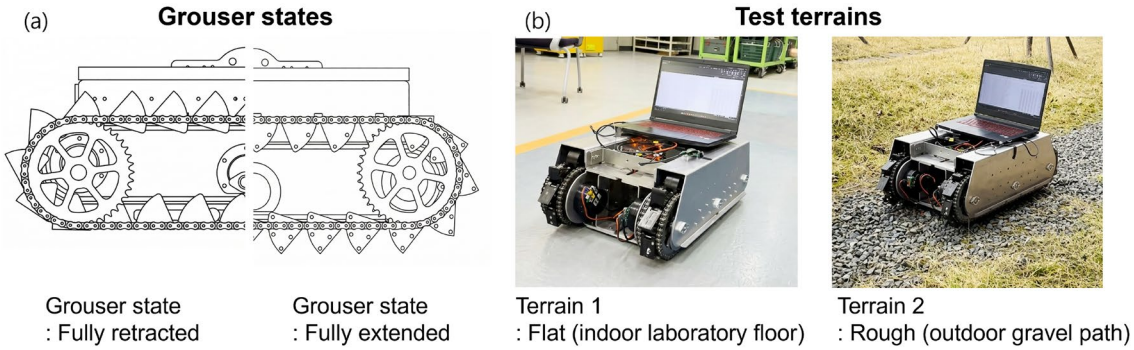

Fig. 13. Robot platform for Experiment 2. (**a**) Two states of the track grouser. (**b**) Driving tests on flat and rough terrains.

This distinguishes EATbot from wheel-legged systems that climb stairs through discrete leg-like or wheel-shape transformation but often require gait planning, additional joints, or mode-specific locomotion strategies.

Overall, the experimental observations are consistent with the theoretically predicted climbable region in Fig. 10. The results demonstrate that stair-climbing capability is governed by discrete grouser spacing compatibility, distributed contact tolerance, and the geometric transformation limit. Together with the comparative results in Table 2, the experimentally verified maximum inclination of 48.85° indicates that the proposed transformable grouser profile enables high-inclination stair engagement within a compact tracked platform.

Experiment 2: driving stability evaluation on flat and rough terrain

Objective

Following the stair-climbing characterization in Experiment 1, this experiment evaluates terrain-dependent driving stability during continuous locomotion. As shown in Fig. 4, the proposed mechanism can continuously deploy and retract the arc grousers between the retracted and maximum-protrusion configurations. The objective of this experiment is to quantify the fixed-grouser-profile trade-off by locking this continuous protrusion range at its two bounding configurations and comparing their driving stability under flat and rough terrain conditions, as shown in Fig. 13. Thus, the two locked configurations are used as controlled fixed-profile baselines, not as the only operating states of the proposed mechanism.

Experimental procedure

To emulate fixed-profile track conditions under identical hardware conditions, the transformable grouser mechanism was tested in two locked configurations. The retracted-locked state represents a low-protrusion fixed-track baseline, whereas the extended-locked state represents a high-protrusion fixed-grouser baseline. These two locked states correspond to the lower and upper bounds of the continuous protrusion range demonstrated in Fig. 4, and were selected to maximize the observable difference between flat-ground smoothness and rough-terrain engagement.

In conventional fixed-profile tracks, the outer tread or grouser geometry is mechanically fixed by the track structure. Therefore, changing the grouser protrusion condition generally requires replacing or redesigning the track. In contrast, the proposed mechanism can realize both tested fixed-profile limits within the same track module and can continuously modulate grouser protrusion between them. Thus, the two locked configurations are used only as controlled baselines for quantifying the fixed-profile trade-off.

Because both baselines were implemented using the same robot platform, differences in mass, drivetrain, controller, sensor placement, and track geometry other than grouser protrusion were eliminated. Therefore, this same-platform comparison isolates the effect of grouser protrusion on terrain-dependent vibration response more directly than comparing different robots or separately manufactured tracks.

For each terrain condition, straight driving tests were conducted under identical velocity commands. Each configuration was tested in three repeated trials to ensure statistical reliability. All experiments were performed using the same robot platform and control parameters.

An external E2BOX IMU was mounted at the chassis center. Data were transmitted at 115200 baud with a sampling interval of 150 ms. Each measurement frame contained roll, pitch, yaw, and tri-axial accelerations (a_x, a_y, a_z) expressed in units of g.

Signal processing and stability metric

To isolate terrain-induced vibration, the vertical acceleration signal was high-pass filtered using a second-order Butterworth filter with cutoff frequency $f_c = 0.5$ Hz:

$$a_{z,\mathrm{HP}}(t) = \mathrm{HP}\{a_z(t)\}. \tag{17}$$

Driving stability was quantified using the root mean square (RMS) of the filtered signal:

$$\mathrm{RMS}(a_{z,\mathrm{HP}}) = \sqrt{\frac{1}{N}\sum_{i=1}^{N} a_{z,\mathrm{HP}}(i)^2}. \tag{18}$$

Lower RMS values indicate reduced vibration energy and improved chassis stability.

Results

The experimental results are summarized in Fig. 14.

On flat terrain (Fig. 14a,b), the retracted-locked configuration, corresponding to the low-profile fixed-configuration baseline, produced slightly lower vibration levels than the extended-locked configuration. The RMS value decreased by approximately **5.1%** (three repeated trials, mean ± s.d.), indicating that minimizing protrusion improves ride smoothness on rigid surfaces. The relatively small difference suggests that internal drivetrain excitation dominates the vertical response when ground irregularity is minimal.

In contrast, on rough step terrain (Fig. 14c,d), the extended-locked configuration, corresponding to the high-profile fixed-grouser baseline, significantly reduced vibration. The RMS decreased by approximately **87.9%** compared to the low-profile fixed-configuration baseline under identical driving speed. The large reduction demonstrates that grouser protrusion substantially alters contact mechanics on uneven terrain, improving anchoring and reducing impact-induced vertical excitation. The standard deviation across repeated trials remained small, confirming repeatability.

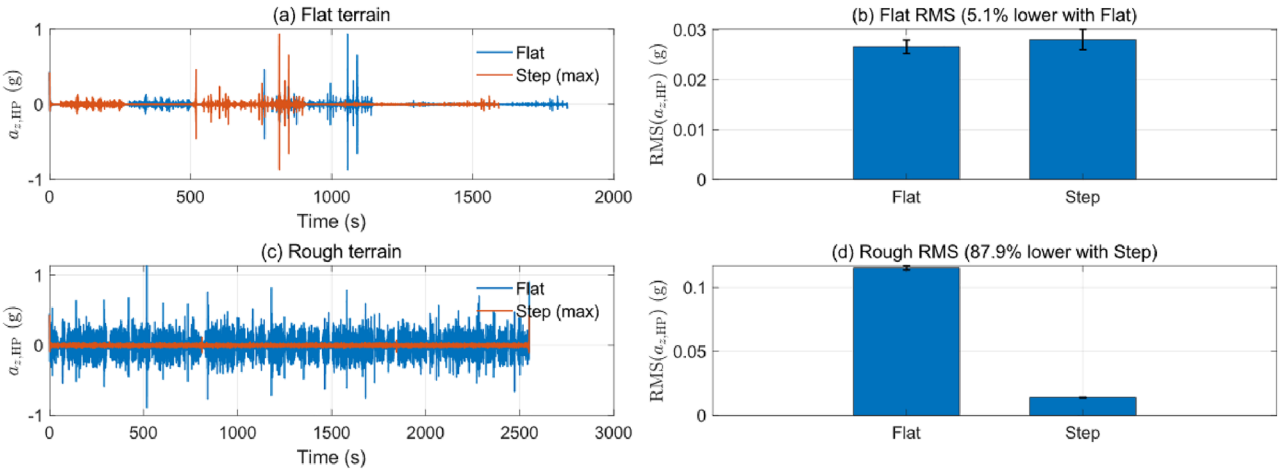

Fig. 14. Driving stability comparison on flat and rough terrain. (**a**,**c**) Representative high-pass filtered vertical acceleration signals $a_{z,\mathrm{HP}}(t)$ during straight driving. (**b**,**d**) RMS vibration levels (mean ± s.d.) for each grouser configuration.

Discussion

The results reveal a clear terrain-dependent trade-off between low-protrusion and high-protrusion fixed-profile configurations. On flat terrain, the retracted-locked baseline produced slightly lower vibration, indicating that reduced protrusion is beneficial when ground irregularity is small. On rough step terrain, the extended-locked baseline substantially reduced vibration by improving terrain engagement and reducing impact-induced vertical excitation.

These findings show that a single fixed grouser profile is unlikely to provide the best vibration response across both smooth and rough terrain. In conventional fixed-profile tracks, this trade-off is inherent because the outer tread or grouser geometry is fixed. If a different protrusion condition is required for another terrain, the track geometry itself must generally be changed by replacing or redesigning the track. In contrast, the proposed mechanism can realize both low-protrusion and high-protrusion fixed-profile limits within the same track module and can continuously adjust grouser protrusion between these limits, as demonstrated in Fig. 4.

Therefore, Experiment 2 does not imply that the proposed mechanism has only two operating states. Instead, the two extreme locked states were used to clearly quantify the fixed-profile trade-off at the lower and upper bounds of the continuous protrusion range. Together with the stair-climbing result in Experiment 1, these results show that grouser protrusion strongly affects both flat-ground driving smoothness and rough-terrain/stair engagement. Thus, the advantage of EATbot lies in its ability to retain a single continuous-track platform while adapting the effective grouser protrusion to different terrain conditions.

Experiment 3: payload transformation and torque evaluation

Objective

This experiment evaluates whether the proposed grouser mechanism can complete its transformation under external payload conditions and whether the required transformation torque remains within the actuator's capability. The test was not intended to determine the ultimate failure load of the mechanism because destructive loading could damage the prototype. Instead, payloads up to 40 kg were applied to examine the functional feasibility of the transformation mechanism under practical loading conditions. The 40 kg payload was selected as a self-weight-level load comparable to the robot's weight.

The objective of this experiment is therefore twofold:

(1) to verify that the grouser mechanism can transform from the retracted configuration to the fully deployed configuration under payload conditions, and
(2) to evaluate the transformation torque estimated from actuator current measurements and compare it with the actuator capability limits.

Experimental setup

Payloads of 0, 10, 20, 30, and 40 kg were sequentially mounted on the robot body. Representative configurations at 0 kg and 40 kg are shown in Fig. 15. For each payload condition, the mechanism was commanded to transform from the retracted grouser configuration to the fully deployed grouser configuration. Each payload condition was repeated three times under identical transformation commands.

Motor current data, denoted as Current_M1 and Current_M2, were recorded from the two T-motor transformation actuators at the driver level. The actuators were coupled to the eccentric shaft through a 5:1 external gear reduction. Assuming a conservative gearbox efficiency of $\eta_g = 0.85$, the transformation torque at the eccentric shaft was estimated from the measured current as

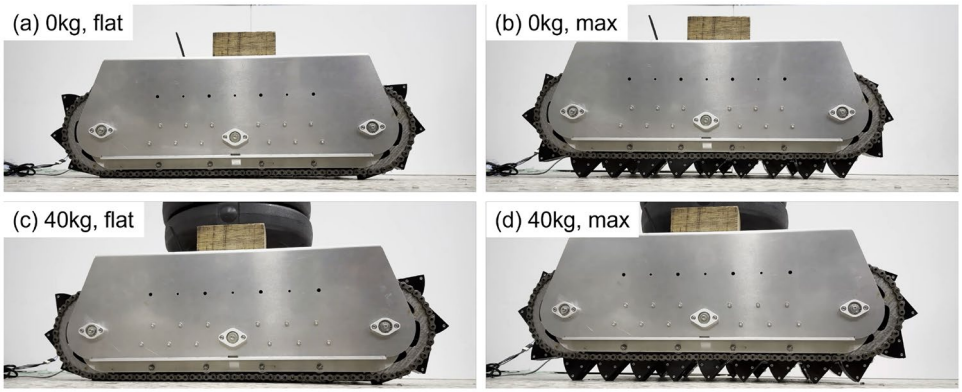

Fig. 15. Payload transformation test of the proposed track module. (**a**,**b**) Transformation without payload from the retracted grouser configuration to the fully deployed grouser configuration. (**c**,**d**) Transformation under a 40 kg payload from the retracted grouser configuration to the fully deployed grouser configuration. The 40 kg payload was selected as a practical self-weight-level load, and the successful transformation demonstrates the functional feasibility of the grouser mechanism under the tested payload condition.

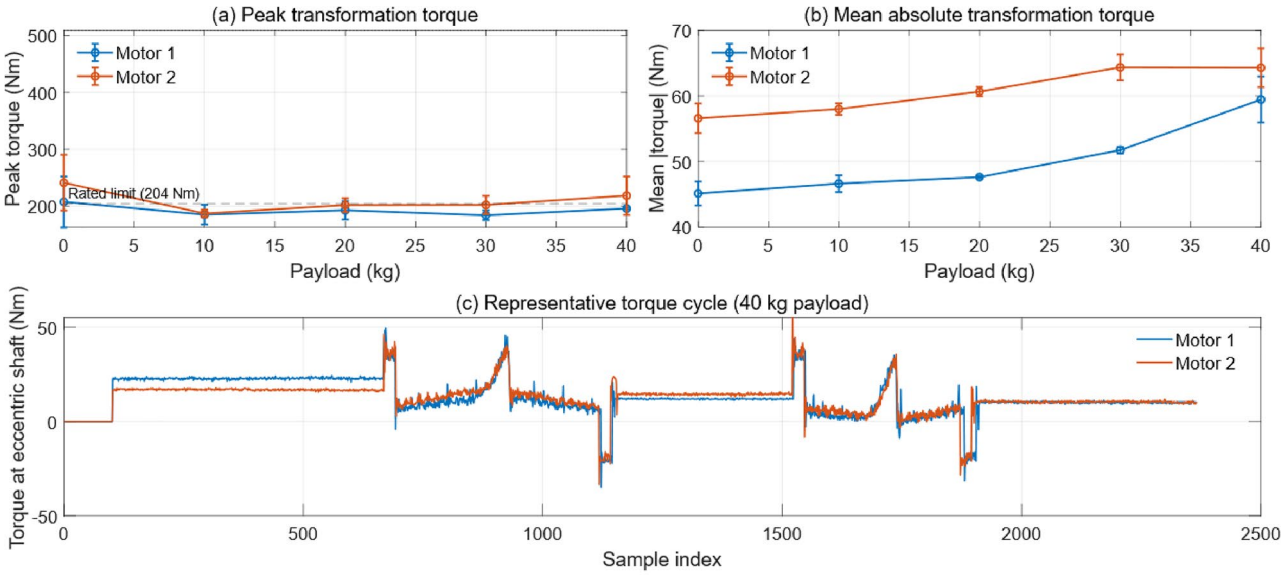

Fig. 16. Transformation torque evaluation under payload conditions. (**a**) Peak transformation torque at the eccentric shaft for payloads of 0–40 kg. (**b**) Mean absolute transformation torque for the same payload conditions. (**c**) Representative torque profile during a full transformation cycle under the 40 kg payload condition. Error bars indicate the standard deviation over three repeated trials. The horizontal reference line in (**a**) indicates the rated actuator torque limit.

$$\tau_{\mathrm{ecc}} = 5\eta_g \left(\frac{120}{19}\right) I, \tag{19}$$

where 120 Nm and 19 A correspond to the peak torque and peak current of the T-motor actuator, respectively. This yields an effective torque constant of approximately 26.8 Nm/A at the eccentric shaft.

Results

As shown in Fig. 15, the grouser mechanism successfully completed the transformation from the retracted configuration to the fully deployed configuration under both the no-payload and 40 kg payload conditions. No visible structural failure, actuator stall, or abnormal mechanical interference was observed during the transformation. This result confirms that the mechanism can maintain its transformation function under the tested self-weight-level payload condition.

The measured transformation torque results are shown in Fig. 16. The peak torque at the eccentric shaft remained near the rated actuator torque limit over the tested payload range, as shown in Fig. 16a. Although local peak values approached the rated limit, they remained below the peak actuator capability, indicating that the transformation actuator retained sufficient short-duration torque margin during the tested transformation cycles.

The mean absolute transformation torque increased with payload, as shown in Fig. 16b. This trend indicates that the external payload increases the average torque demand during grouser transformation. The representative time-domain torque profile for the 40 kg payload case is shown in Fig. 16c. The torque profile contains transient peaks during the transformation phases, whereas the torque remains comparatively stable during intermediate holding periods.

Overall, the payload transformation test and torque evaluation show that the proposed mechanism can perform the required retracted-to-deployed transformation under payloads up to 40 kg. Because the test was limited to a practical self-weight-level payload, the result should be interpreted as a functional feasibility verification rather than an ultimate payload-capacity measurement. Together with the CAE-based structural verification, these results support the feasibility of the load-bearing transformation mechanism under the tested payload conditions.

Conclusion

This study proposed EATbot, an environment-adaptive tracked robot featuring a protrusion-maximized continuously transformable arc-grouser mechanism. Unlike conventional fixed-profile tracks, the proposed mechanism focuses on the grouser as the primary ground-contact element and continuously modulates its protrusion/contact profile over the range from the retracted configuration to the maximum-protrusion configuration. This enables a single track module to realize both flat-ground-friendly and high-engagement contact conditions, as well as continuous configurations between them, while preserving the continuous-contact characteristics of tracked locomotion.

The arc-grouser geometry and eccentric guide mechanism were designed under chain-pitch discretization, internal interference, packaging, grouser curvature, and actuator feasibility constraints. The eccentric non-collinear coupled linkage separates the dead-center input angles of the coupled sub-loops, preventing simultaneous dead-center locking in the implemented mechanism. The kinematic model, virtual-work-based torque formulation, and finite element analysis clarify the geometric, actuation, and structural feasibility of the proposed grouser-transformation mechanism.

The experiments quantitatively characterized the performance, trade-off mitigation, and practical feasibility of the implemented prototype. Stair-climbing tests verified the predicted climbable domain and demonstrated successful ascent up to an equivalent inclination of 48.85°, confirming the benefit of the protrusion-maximized arc-grouser profile for severe stair-edge engagement. Driving stability tests using same-platform locked configurations showed that the retracted profile reduced vibration on flat terrain, whereas the maximum-protrusion profile reduced vibration on rough terrain. Payload transformation tests up to 40 kg further confirmed that the mechanism can complete the required transformation under practical self-weight-level loading.

The present prototype demonstrates hardware-level adaptability of the track–terrain contact profile through continuous grouser-profile transformation. Autonomous terrain recognition, online decision-making, and closed-loop grouser-profile control were not included in the current prototype and will be addressed in future work. Overall, the proposed mechanism provides a grouser-focused approach to adaptive tracked locomotion by mitigating the fixed-grouser-profile trade-off within a single continuous-track platform.

Data availability

Raw experimental data and supplementary materials are provided in the Supplementary Information and Supplementary Data files.

Received: 28 February 2026; Accepted: 7 July 2026
Published online: 17 July 2026

References

1. Bruzzone, L. & Quaglia, G. Locomotion systems for ground mobile robots in unstructured environments. *Mech. Sci.* **3**, 49–62 (2012).
2. Kajita, S. & Espiau, B. Legged robot. In *Springer Handbook of Robotics*, 361–389 (Springer Berlin/Heidelberg, 2008).
3. Raibert, M. H. *Legged Robots that Balance* (MIT Press, 1986).
4. Morin, P. & Samson, C. Motion control of wheeled mobile robots. *Spring. Handb. Robot.* **1**, 799–826 (2008).
5. De Luca, A., Oriolo, G. & Vendittelli, M. Control of wheeled mobile robots: An experimental overview. In *RAMSETE: Articulated and Mobile Robotics for Services and Technologies*, 181–226 (2002).
6. Iwamoto, T. & Yamamoto, H. Mechanical design of variable configuration tracked vehicle. *J. Mech. Des.* **112**, 289–294. https://doi.org/10.1115/1.2912606 (1990).
7. Bruzzone, L., Nodehi, S. E. & Fanghella, P. Tracked locomotion systems for ground mobile robots: A review. *Machines* **10**, 648 (2022).
8. Budiharto, W. Design of tracked robot with remote control for surveillance. In *Proceedings of the 2014 International Conference on Advanced Mechatronic Systems*, 342–346 (IEEE, 2014).
9. Choi, B. et al. Development and control of a military rescue robot for casualty extraction task. *J. Field Robot.* **36**, 656–676 (2019).
10. Budiharto, W., Andreas, V., Suroso, J. S., Gunawan, A. A. S. & Irwansyah, E. Development of tank-based military robot and object tracker. In *2019 4th Asia-Pacific Conference on Intelligent Robot Systems (ACIRS)*, 221–224 (IEEE, 2019).
11. Bertrand, R., Schaefer, B., Van Winnendael, M. & Rieder, R. European tracked micro-robot for planetary surface exploration. *IFAC Proc. Vol.* **31**, 37–44 (1998).
12. Kalita, H. & Thangavelautham, J. Exploration of extreme environments with current and emerging robot systems. *Curr. Robot. Rep.* **1**, 97–104 (2020).
13. Dong, P., Wang, X., Xing, H., Liu, Y. & Zhang, M. Design and control of a tracked robot for search and rescue in nuclear power plant. In *2016 International Conference on Advanced Robotics and Mechatronics (ICARM)*, 330–335 (IEEE, 2016).
14. Ducros, C. et al. Rica: A tracked robot for sampling and radiological characterization in the nuclear field. *J. Field Robot.* **34**, 583–599 (2017).
15. Higa, S., Nagaoka, K. & Yoshida, K. Stress distributions of a grouser wheel on loose soil. *J. Terrramech.* **85**, 15–26 (2019).
16. Suzuki, H., Watanabe, Y., Kobayashi, T., Iagnemma, K. & Ozaki, S. Terramechanics-based investigation of grouser shape for rigid wheels: Comparison between rectangular and trapezoidal grousers. *Cogent Eng.* **7**, 1846254 (2020).
17. Wang, L., Chen, X., Wang, L., Li, Z. & Yang, W. Mechanical properties and soil failure process of interface between grouser of tracked mining vehicle and deep-sea sediment. *Ocean Eng.* **285**, 115336 (2023).
18. Griffo, V. & Nakka, Y. K. Terrain-adaptive grouser wheel for optimal planetary exploration: Design and experimental investigation. arXiv preprint arXiv:2605.24311 (2026).
19. Kim, Y. et al. Step: A new mobile platform with 2-dof transformable wheels for service robots. *IEEE/ASME Trans. Mechatron.* **25**, 1859–1868 (2020).
20. Landersa, V. S., Ranasingheb, S. B., Pathiranac, R. O. & Peirisd, J. T. A self adapting wheel system for space exploration rovers. *Int. Astron. Congr.* (2021).
21. Chen, Y., Kamioka, A., Iwase, M., Inoue, J. & Satoh, Y. Design and analysis of transformable wheel with pivoting-head mechanism. *Appl. Mech.* **4**, 70–89 (2023).
22. International Code Council (ICC). 2017 icc a117.1 accessible and usable buildings and facilities. Tech. Rep., ICC Digital Codes (2017). https://codes.iccsafe.org/content/icca117-12017P4/chapter-5-general-site-and-building-elements (accessed 9 May 2023).
23. Ministry of Land, Infrastructure and Transport. Rules on standards for evacuation and fire protection of buildings (2023). https://www.law.go.kr/ (accessed 9 May 2023).
24. Komura, H., Endo, G. & Suzumori, K. Eccentric crank rover: A novel crank wheel mechanism with eccentric wheels. In *Proc. IEEE/RSJ Int. Conf. Intell. Robots Syst.*, 1048–1053 (2016).
25. Park, S. et al. Wave: Last mile delivery robotic platform with stair-climbing ability via four-bar linkage-based locomotion. *IEEE/ASME Trans. Mechatron.* **29**, 313–323 (2023).
26. Han, J. & Shi, S. A novel methodology for determining the singularities of planar linkages based on Assur groups. *Mech. Mach. Theory* **147**, 103751 (2020).
27. Tsai, C. & Wang, L. On the dead-centre position analysis of Stephenson six-link linkages. *Proc. Inst. Mech. Eng. C J. Mech. Eng. Sci.* **220**, 1393–1404 (2006).

28. Chen, S.-C. et al. Quattroped: a leg-wheel transformable robot. *IEEE/ASME Trans. Mechatron.* **19**, 730–742 (2013).
29. Zheng, C., Sane, S., Lee, K., Kalyanram, V. & Lee, K. α-waltr: Adaptive wheel-and-leg transformable robot for versatile multiterrain locomotion. *IEEE Trans. Rob.* **39**, 941–958 (2022).
30. Yamada, Y. & Nakamura, T. Gerwalk: Lightweight mobile robot with buoyant balloon body and bamboo rimless wheel. In *2018 IEEE International Conference on Robotics and Biomimetics (ROBIO)*, 1814–1821 (IEEE, 2018).
31. Li, I.-H., Wang, W.-Y. & Tseng, C.-K. A kinect-sensor-based tracked robot for exploring and climbing stairs. *Int. J. Adv. Rob. Syst.* **11**, 80 (2014).
32. Mostyn, V., Krys, V., Kot, T., Bobovsky, Z. & Novak, P. The synthesis of a segmented stair-climbing wheel. *Int. J. Adv. Rob. Syst.* **15**, 1729881417749470 (2018).
33. Park, S., Shin, J., Kim, Y. & Seo, T. Waves: Soft-material based adaptable walking-type stair-climbing robot for various step sizes. *IEEE Access* **12**, 13100–13111 (2024).
34. Sasaki, K. & Suzuki, K. Active rotary-legs mechanism for stair-climbing mobility vehicle. *IEEE Robot. Autom. Lett.* **3**, 2237–2244 (2018).
35. Dalvand, M. M. & Moghadam, M. M. Stair climber smart mobile robot (msrox). *Auton. Robot.* **20**, 3–14 (2006).
36. Seo, T., Ryu, S., Won, J. H., Kim, Y. & Kim, H. S. Stair-climbing robots: A review on mechanism, sensing, and performance evaluation. *IEEE Access* **11**, 60539–60561 (2023).

Author contributions

H.K. conceived the study and led the design, analysis, experiments, and manuscript preparation. Y.K. and H.S. contributed to design, fabrication, and system implementation. J.Y., S.K., and J.K. conducted experiments and data analysis. T.S. supervised the research and served as the corresponding author. All authors reviewed and approved the manuscript.

Funding

This research was supported by the National Research Foundation of Korea (NRF) Grant funded by the Ministry of Science and ICT for the Bridge Convergence *R* & *D* Program (RS-2024-00421129) and by the "Regional Innovation System & Education (RISE)" through the Seoul RISE Center, funded by the Ministry of Education (MOE) and the Seoul Metropolitan Government (2025-RISE-01-027-04).

Declarations

Competing interests

The authors declare no competing interests.

Additional information

Supplementary Information The online version contains supplementary material available at https://doi.org/10.1038/s41598-026-61685-2.

Correspondence and requests for materials should be addressed to T.S.

Reprints and permissions information is available at www.nature.com/reprints.

Publisher's note Springer Nature remains neutral with regard to jurisdictional claims in published maps and institutional affiliations.

Open Access This article is licensed under a Creative Commons Attribution-NonCommercial-NoDerivatives 4.0 International License, which permits any non-commercial use, sharing, distribution and reproduction in any medium or format, as long as you give appropriate credit to the original author(s) and the source, provide a link to the Creative Commons licence, and indicate if you modified the licensed material. You do not have permission under this licence to share adapted material derived from this article or parts of it. The images or other third party material in this article are included in the article's Creative Commons licence, unless indicated otherwise in a credit line to the material. If material is not included in the article's Creative Commons licence and your intended use is not permitted by statutory regulation or exceeds the permitted use, you will need to obtain permission directly from the copyright holder. To view a copy of this licence, visit http://creativecommons.org/licenses/by-nc-nd/4.0/.

© The Author(s) 2026